ChemPubSoc Europe

DOI: 10.1002/celc.201600064

CHEMELECTROCHEM Articles

On the Importance of Regulating Hydroxyl Coverage on the Basal Plane of Graphene Oxide for Supercapacitors

Alexander J. Pak and Gyeong S. Hwang*[a]

Reduced graphene oxide (rGO) has been explored as an alternative to graphene as an electrode material for use in supercapacitors, which thus enables highly scalable solution-based processing. To understand the performance of rGO electrodes in supercapacitors, we theoretically investigate model systems by considering OH-functionalized graphene immersed in 1-ethyl-3-methylimidazolium bis(fluorosulfonyl)imide (EMIM/FSI) ionic liquid. Our specific interest is to understand the influence of varying the hydroxyl content (or O/C ratio) on both the quantum (C_Q) and electric double-layer (C_D) capacitances. Ultimately, the total interfacial capacitance is found to be sensitive to O/C, but is optimized when the suppression of C_D is most effectively mitigated by the enhancement in C_Q. Our findings clearly demonstrate that the use of GO materials has the potential to enhance supercapacitor performance significantly but will require careful control of both the concentration and composition of oxygen functional groups along the basal surface.

1. Introduction

Electrochemical double-layer capacitors (EDLCs), otherwise known as supercapacitors, are energy-storage devices that are well suited for high-power applications due to their large power density and long cycling lifetimes.[1,2] However, the ubiquitous adoption of supercapacitors has been curtailed by their characteristically low specific and volumetric energy densities. To mitigate this limitation, both the operating voltage and the capacitance can be improved through careful consideration of the electrode and electrolyte materials. For the latter, ionic liquids have shown promise owing to their wide electrochemical window (i.e. large operating voltage), high thermal stability, and low vapor pressure.[3,4] For the former, graphene-based materials have emerged as a potential electrode candidate; their large specific surface area and excellent electrical conductivity are favorable for enhanced double-layer capacitance.[3,4–7] However, many challenges still need to be addressed. For example, the intrinsically low quantum capacitance of graphene can limit the overall performance.[8–15] In addition, the prevention of graphene sheet restacking to access the large surface area remains a costly and difficult process.[16]

In recent years, reduced graphene oxide (rGO) has gained popularity as an alternative graphene-based material. Part of the attraction is the cost-effective means of producing rGO from the wet exfoliation of graphene oxide and subsequent chemical, thermal, or electrochemical reduction.[17–19] Although rGO has traditionally been used as a precursor for graphene sheets,[19] rGO is also an interesting and important material in its own right. For example, the oxygen moieties serve as electrochemically active sites that have been used for enhanced catalytic activity of oxygen reduction[20] and pseudo-capacitive benefits in aqueous EDLCs.[21–23] Naturally, rGO has also been explored for use as an electrode material in supercapacitors with organic or ionic-liquid electrolytes that are electrochemically stable. To date, however, experimental results that probe the advantages of rGO for EDLC applications are widely scattered. Although rGO electrodes have been shown to outperform graphene electrodes,[24,25] reported capacitances have exhibited contradictory sensitivities to the ratio of oxygen to carbon atoms (O/C) and the reduction process.[26,27] This underscores the need to understand the influence of the extent of reduction on the capacitance.

To evaluate the impact of rGO reduction on EDLC performance, it is important to recognize that the total interfacial capacitance (C_T) strongly depends upon the contributions from the electrode quantum capacitance (C_Q) and electric double-layer (EDL) capacitance (C_D).[8–12] Although the latter property primarily depends upon the accumulation of ions at the interface, the former quantifies the ease by which excess charge carriers populate the electronic states of the electrode. To decouple these contributions, theoretical simulations can provide valuable insights. For example, molecular dynamics simulations have shown that regularly dispersed coverage of the basal plane of graphene with hydroxyl (OH) or epoxide functional groups tends to monotonically decrease C_D as the moiety content increases.[28–30] Quantum mechanical calculations have also shown that C_Q can be dramatically enhanced through OH functionalization of edge sites[31] and chemical modification of basal sites,[11,32] although the basal-plane coverage by OH has yet to be studied in this context. However, one challenge in undertaking such a fundamental investigation is a proper account of the rGO structure. Experimental characterizations by using NMR spectroscopy and X-ray photoelectron spectrome-

[a] A. J. Pak, Prof. G. S. Hwang
Department of Chemical Engineering, University of Texas
Austin, Texas 78712 (USA)
E-mail: gshwang@che.utexas.edu

Supporting Information for this article can be found under http://dx.doi.org/10.1002/celc.201600064.

try have identified the presence of several oxygen moieties, such as OH, epoxide, carboxyl, and carbonyl groups, although the first two (OH and epoxide) are generally identified as the most common species on the basal surface.[33,34] Furthermore, recent experimental[35,36] and theoretical[37,38] work has shown that oxygen moieties tend to aggregate along the basal surface and form distinct graphitic and oxidized regions. Therefore, careful attention should be applied in theoretical studies to account for such structures. To this end, one possible method is a lattice-based Monte Carlo scheme, such as the one used by Zhou and Bongiorno.[37]

Herein, we investigate the effect of varying the O/C of rGO electrodes on C_T in comparison to that of pristine graphene. We only consider the OH functionalization of the basal surface of graphene for simplicity and account for possible agglomeration by using lattice-based Monte Carlo simulations. First, we employed density functional theory (DFT) and density functional tight binding (DFTB) theory to study the electronic structure (C_Q) and electrochemical stability of the rGO sheets. Then, we used classical molecular dynamics (MD) to study the microstructure and C_D of the electrodes immersed in 1-ethyl-3-methylimidazolium bis(fluorosulfonyl)imide ([EMIM][FSI]), an ionic liquid with a wide electrochemical window (4.5 V with respect to glassy carbon), low viscosity, and good ionic conductivity.[39,40] Our results demonstrate that the performance of supercapacitors by using rGO electrodes depends upon the competition between C_Q and C_Q, but can vastly outperform pristine graphene electrodes. This study motivates future investigations into the control and careful optimization of the oxygen content to balance the oxygen-induced influences on C_Q and C_D.

2. Results and Discussion

2.1. Electronic Structure and Quantum Capacitance

In this section, the electronic structure of rGO is reported at different OH contents (i.e. O/C ratio). First, the electronic density of states (DOS) of rGO at O/C ratios of 0.054 and 0.268 were analyzed by using DFT–GGA. Next, the viability of using the DFTB approach in place of DFT–GGA is demonstrated. By using DFTB, we then proceeded to calculate the influence of O/C on the integral C_Q of rGO.

Figure 1a depicts the total DOS of a rGO sheet with an O/C ratio of 0.054. The sharp peaks seen above the Fermi level (E_F) ($0 < E - E_F < 0.4$ eV) are indicative of the quasi-localization of states that arises from the presence of OH groups, which is similarly present in graphene with chemical dopants[11,32] and topological defects.[12,41] As seen from the band-decomposed charge density isosurfaces of regions I and II, the quasi-localized states near E_F are primarily associated with the p_z states of C atoms near to OH moieties, at which the π system is most distorted; note that we find the O 2p states to be 1.8 eV below E_F (shown in Figure S2 in the Supporting Information). For an O/C ratio of 0.268 (Figure 1b), the density of quasi-localized states near E_F is found to increase because the distortion to the π system intensifies with the addition of more OH groups; here, a gap of 0.28 eV is also predicted to appear.

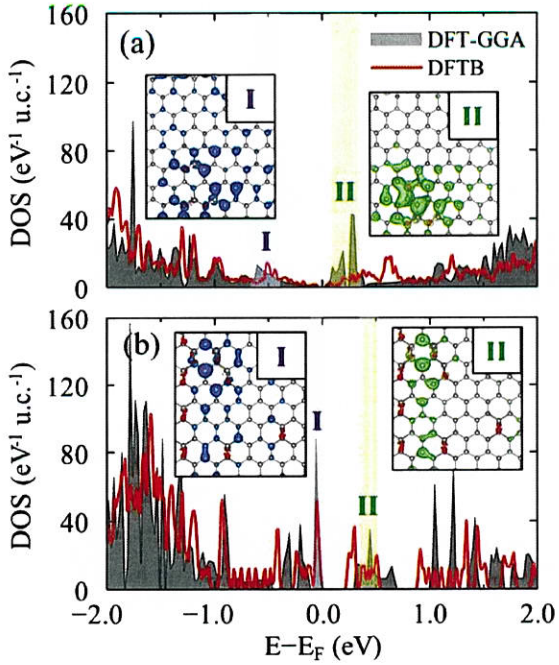

Figure 1. The density of states (DOS) of rGO with respect to the Fermi level (E_F) for O/C ratios of a) 0.054 and b) 0.268, as calculated by using the listed quantum mechanical methods. Insets: The band-decomposed charge-density isosurfaces (0.001 e bohr^{-3}) for highlighted regions I and II, in which blue and green isosurfaces correspond to electrons and holes, respectively.

The presence of OH moieties consequently influences the charge distribution across the rGO sheet. As expected, the OH moieties withdraw electrons from the π system and thus act as a p-type dopant; therefore, the adjacent C atoms are electropositive (as depicted in the charge distribution map in Figure S3). We can also expect excess charge carriers to primarily fill the π system, with slight accumulation near the OH sites at which the degree of quasi-localization is largest (see Figure S4). Later, we will discuss the implications of the resultant charge redistribution on the electrode–electrolyte interactions at the interface.

Because our goal is to investigate the electronic structure of large and disordered sheets of rGO with as many as thousands of atoms in a unit cell, we now consider the efficacy of an alternative and less expensive computational method. In Figure 1a, b, we compare the DOS predicted by DFT–GGA to that of DFTB and find that the latter sufficiently approximates the former. However, it is clear that the DFTB method systematically underestimates the electronic localization relative to DFT–GGA. For example, for an O/C ratio of 0.054, the empty states in the DFTB DOS are broadened such that the peak appears around 0.3 eV above its relative position predicted by using DFT–GGA. Furthermore, the bandgap for the O/C ratio of 0.268 is predicted to be 0.06 eV smaller by the DFTB calculation. Nonetheless, DFTB captures the general availability of states near E_F, which ultimately determines C_Q (for pristine graphene, refer to Figure S5). Herein, we will use DFTB to estimate the DOS of rGO with varying O/C values.

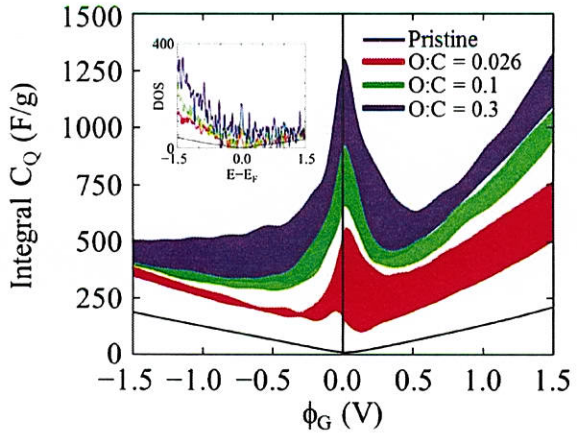

Figure 2. Comparison of the integral quantum capacitance (C_Q) for pristine graphene and rGO with the listed O/C ratios at varying local electrode potential (ϕ_G). The width of the profiles corresponds to the standard deviation of the mean sampled over five different rGO configurations. The inset shows the corresponding DOS [eV^{-1} u.c.$^{-1}$] with respect to $E-E_F$ [eV].

Figure 2 shows the integral C_Q as a function of local electrode potential (ϕ_G) calculated for larger rGO sheets (41.9288 × 42.7193 Å^2) with O/C ratios of 0.026, 0.1, and 0.3 and for pristine graphene; details on the preparation and analysis of the rGO structure can be found in the provided Supporting Information. By using DFTB+ simulations, C_Q was computed based on the procedure described in Ref. [10] from the DOS averaged over all samples (Figure 2, inset). Compared with pristine graphene, the overall C_Q of the rGO sheets tends to increase as O/C increases, especially close to the charge-neutrality point, which reflects the additional availability of states that results from the disruption of the π system by OH groups; note that C_Q can vary as much as $\pm 125\ F\,g^{-1}$ due to different configurations of OH moieties. Furthermore, it is evident that the OH-induced enhancement in C_Q tends to be more dramatic with positive polarity. Interestingly, our calculations predict that rGO remains metallic at an O/C ratio of 0.3. In the absence of structural defects, this may be reasonable because the percolation threshold of thermally reduced GO was found to be around O/C 0.2.[42] However, recall that if an O/C ratio of 0.268 is used in the above calculation, we observe a bandgap of 0.22 to 0.28 eV. These conflicting results suggest that the bandgap in the latter case may be induced by a super-lattice effect, owing to the smaller supercell size.

To test the super-lattice effect, we calculate the electronic structure of rGO with homogeneously dispersed OH moieties across the basal surface and predict a bandgap of 0.45 eV (Figure S6). This opening of a bandgap is akin to the Robertson and O'Reilly model, in which the optical gap of amorphous carbon varies inversely with the size of homogeneous sp^2 clusters.[43] Thus, we can attribute the emergence of the large bandgap to the regularity of the disruption and subsequent confinement of aromatic regions by OH moieties. In the aforementioned rGO sheets constructed with a smaller supercell size, favorable OH moiety configurations can accommodate less agglomeration (i.e. more homogeneous dispersion) due to the periodic images and therefore result in a bandgap. In contrast, the agglomeration of OH moieties in the larger supercell results in separate and contiguous functionalized and graphitic domains, in which the π system remains well coupled and metallic (refer to Figure S1). These results indicate that the electronic structure of rGO sheets can be quite sensitive to the spatial distribution of O species, in addition to their concentrations.

Finally, we discuss the possible irreversible loss of OH moieties from the basal surface upon cycling. In ILs (and other nonaqueous electrolytes), we propose that OH can be reduced to form an OH^- anion, which subsequently extracts a H^+ from adjacent OH groups to form H_2O in the following 1e process [Eqs. (1) and (2)]:

$$rGO-OH + 1\,e^- \rightarrow rGO + OH^- \quad (1)$$

$$OH^- + rGO-OH \rightarrow rGO-O^- + H_2O \quad (2)$$

Unlike buffer solutions, which are traditionally used during electrochemical reduction,[19,44] the H^+ source is limited by the availability of surface OH groups; conceivably, nearby H_2O may also contribute H^+, but we do not consider that case here. Based on this mechanism, the energy of H_2O evolution (ΔE_{evo}) can be computed from the energy difference of the final and initial states ($\Delta E_{evo} = E_{H_2O/O} - E_{GO}$).

Our interest is in evaluating ΔE_{evo} at various O/C ratios by using DFT. We consider the previously used 7×4 rectangular supercells and allow one H_2O to evolve on each side of the rGO sheet; for completeness, the ΔE_{evo} for the neutral, anodic, and cathodic cases are calculated and shown in Figure 3. First, it is evident that at low O/C ratios (0.04), H_2O evolution is favorable and expectedly more so under cathodic potential ($\sigma = -5.43\ \mu C\,cm^{-2}$). However, we find that the evolution becomes increasingly unfavorable as the O/C ratio increases. Therefore, within a fixed operating potential our results suggest that a critical O/C ratio exists, beyond which the loss of OH moieties can be mitigated.

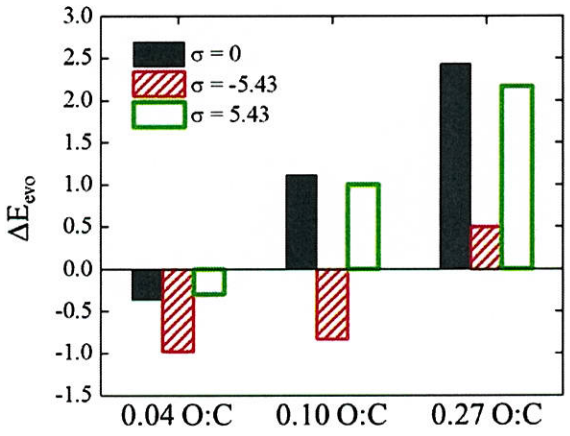

Figure 3. The predicted energy of H_2O evolution (ΔE_{evo}) with various O/C ratios at the listed excess surface charge density (σ [$\mu C\,cm^{-2}$]). The evolution of two H_2O molecules (one on each side of graphene) is considered in all cases.

To understand the origins of this behavior, we refer to our previous electronic structure analysis. Recall that an increase in O/C is commensurate with greater quasi-localization of π states near E_F. Thus, the preferential filling of excess charge carriers in these π states should increase with increased O/C and consequently it is less likely for electrons to localize on an OH site to form OH^-. Note that this behavior should be sensitive to the types of oxygen moieties (such as basal-plane epoxides and edge-plane carboxyls, carbonyls, and lactols) and their relative concentrations, which could be a subject for further study. Nonetheless, this analysis demonstrates that the increased disruption of the π system at increased O/C ratios may enhance both the C_Q and cycling stability of rGO electrodes.

2.2. Electric Double Layer and Capacitance

To evaluate the integral C_D, the microstructure of [EMIM][FSI] near rGO electrodes (O/C 0.1 and 0.3) was investigated and compared with that of pristine graphene electrodes. Here, MD simulations were used to examine how the presence and distribution of OH moieties influences the EDL microstructure across the basal plane and perpendicular to it. Due to the wide electrochemical window of [EMIM][FSI], it is assumed that nonbonding van der Waals (vdW) and Coulomb interactions sufficiently model the interfacial behavior. First, we present the packing behavior of IL ions under neutral conditions. Next, the screening capabilities of the ILs upon electrode charging are discussed. Lastly, we estimate the variation in C_D as a function of O/C.

Figure 4 depicts the two-dimensional (2D) mass density (ρ_m) color map of the first IL layer (thickness $\approx$3.4 Å) under neutral conditions. Near pristine graphene (Figure 4a), the EMIM and FSI ions expectedly pack uniformly across the basal plane. This is further demonstrated in the line profile (Figure 4b), which is nearly flat; note that although FSI has a greater ρ_m due to its larger molecular weight, the number densities of FSI and EMIM are comparable to maintain charge neutrality. Conversely, the EDL exhibits markedly different behavior near the rGO electrodes. The first EDL layer next to the rGO sheet with an O/C ratio of 0.1 (Figure 4c), for example, displays distinct spatial aggregation between EMIM cations and FSI anions. The line profile in Figure 4d further demonstrates that the anions and cations tend to segregate within the 2D plane; this is mainly driven by the aforementioned charge redistribution (Figure S3), such that cations (anions) prefer to aggregate close to the exposed negatively charged O (positively charged H) atoms, which triggers successive alternating packing across the unmodified basal region. As the oxygen surface coverage increases (O/C 0.3 in Figure 4e, f), the 2D segregation becomes noticeably more distinct. We should note that similar 2D structural ordering has also been theoretically demonstrated due to atomically rough substrate surfaces[45] and polarization-induced charge puddles.[46]

The one-dimensional (1D) microstructure perpendicular to the basal plane also displays some differences as the O/C ratio changes. Figure 5a shows the average ρ_m as a function of distance from an uncharged pristine graphene electrode, which exhibits the known oscillatory packing behavior for ILs that dampens away from the electrode;[47–49] the sharp first peak reflects the tendency of both the EMIM and FSI ions to flatten at the interface due to the vdW interaction with the electrode. Similar oscillatory behavior is observed at O/C ratios of 0.1 (Figure 5b) and 0.3 (Figure 5c), although the first peaks tend to broaden; this suggests that some of the ions reorient to screen the charge from the out-of-plane OH groups. In addition, the FSI anions tend to be segregated from the EMIM cations, as indicated by the downshifted position of the EMIM peak with respect to the FSI peak. We can expect a slight preferential accumulation of FSI anions near the basal plane to screen the slightly electropositive C atoms, whereas EMIM prefers to screen the out-of-plane electronegative O atoms.

When the electrodes are charged, it can prove useful to analyze the screening behavior of the IL ions. Based on the charge-density variation (ρ_q), which is proportional to ρ_m (Figures S7 and S8), we can compute the relative screening factor (β_{rel}) [Eq. (3)]:

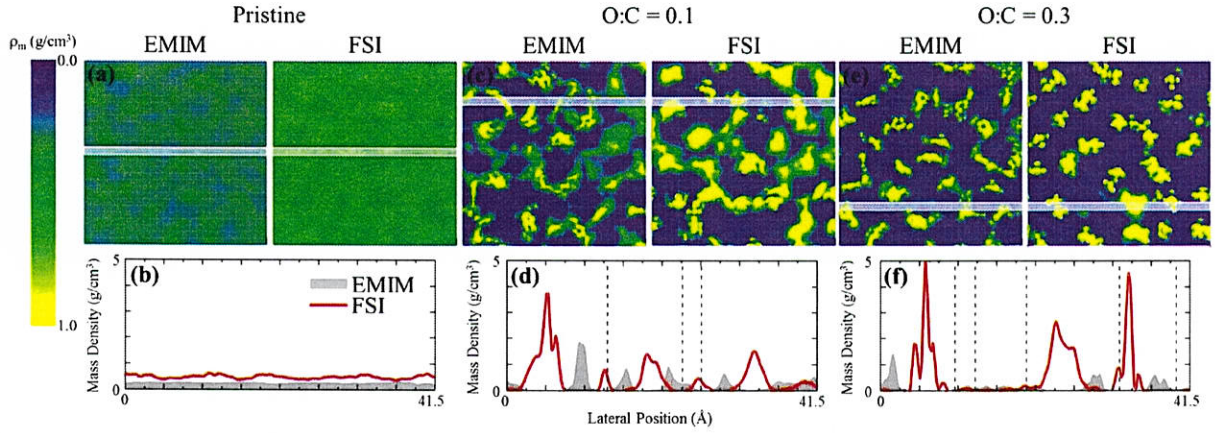

Figure 4. Average two-dimensional mass density (ρ_m) profiles of EMIM and FSI in the first ionic liquid layer for a) pristine, c) O/C 0.1, and e) O/C 0.3 graphene cases, which are shown as color maps. The respective line profiles of the segments along the highlighted region are shown in b), d), and f).

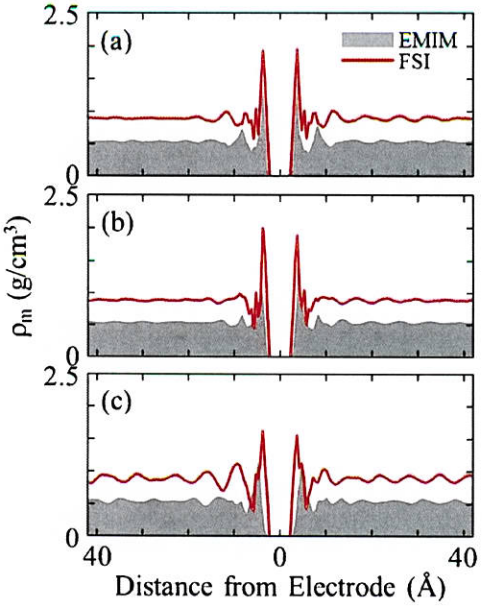

Figure 5. One-dimensional mass density (ρ_m) profiles of EMIM and FSI in the direction perpendicular to the neutral electrode for a) pristine, b) O/C 0.1, and c) O/C 0.3 graphene cases.

$$\beta_{rel} = -\frac{\int_0^z \rho_{q,\sigma} dz - \int_0^z \rho_{q,0} dz}{\sigma} \quad (3)$$

in which $\rho_{q,\sigma}$ and $\rho_{q,0}$ are the charge-density distributions at $|\sigma| > 0$ and $\sigma = 0$ μC cm^{-2}, respectively; because the electrode is screened from both sides, β_{rel} should saturate to a value of 0.5 far away from the electrode.

As seen in Figure 6a, the compact first IL layer near pristine graphene has a peak β_{rel} value of 1.2 at around 4.5 Å when σ is 2.24 μC cm^{-2}. In contrast, the first β_{rel} peak for the O/C ratios of 0.1 and 0.3 cases are respectively broadened and shifted away from the electrode, which indicates that the relative screening capability of the IL ions are increasingly impeded as O/C increases. When σ is −2.24 μC cm^{-2} (Figure 6b), similar behavior is observed in which the peak β_{rel} broadens and diminishes as O/C increases; note, however, that the peak β_{rel} value is around 1.0 (0.6) in the pristine (O/C 0.3) graphene case, which is comparably smaller than the peak β by the positive terminal. These results suggest that the accumulation of counterions at the electrode–electrolyte interface is increasingly unfavorable as O/C increases; in other words, the electrostatic attraction from the excess electrode charge is insufficient to induce the exchange of co-ions for counterions within the 2D segregated microstructure in the first IL layer (Figure 3).

Although β_{rel} offers an intuitive means of quantifying the ease of additional counterion accumulation at the charged electrode interface, it does not reflect the absolute screening capabilities of the IL ions. Instead, we can compute the absolute β (β_{abs}), which is simply the equivalent of Equation (3) without the second term. As depicted in Figure 6a, inset, the β_{abs} peak is largest for a O/C ratio of 0.3 near the positive terminal, which naturally follows the previously demonstrated accumulation of FSI counterions at the rGO interface (Figure 5). The β_{abs} profile near the negative terminal (Figure 6b) also exhibits a valley due to the presence of FSI co-ions. Thus, the decrease in screening capability near the negative polarity as compared with the positive polarity is likely driven by the tendency of the first IL layer to be depleted of EMIM counterions due to FSI accumulation.

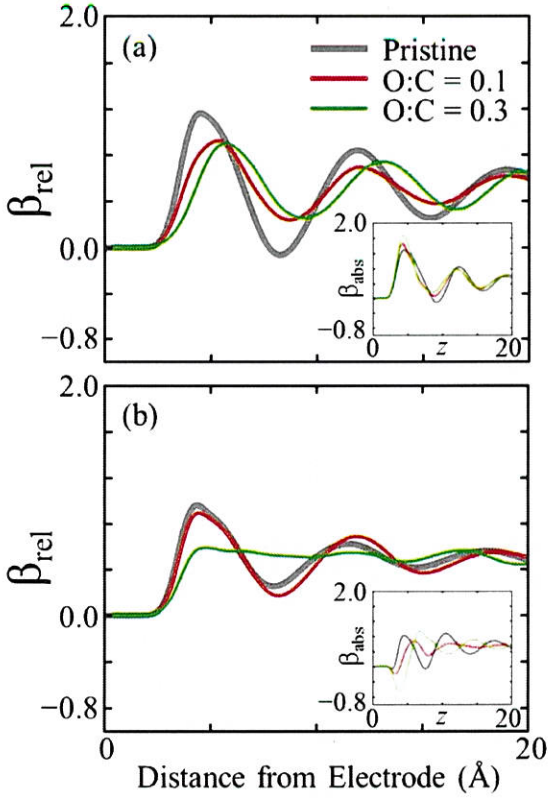

Figure 6. The average relative screening factor (β_{rel}) in the direction perpendicular to the listed electrodes for an excess surface charge density of a) $\sigma = 2.24$ and b) $\sigma = -2.24$ μC cm^{-2}. Insets: The absolute screening factor (β_{abs}) as described in the main text.

Next, the integral C_D is determined from the ratio between σ and the difference between the potential drops across the EDL when charged (ϕ_D) and uncharged (ϕ_Z, i.e. PZC) [$C_D = \sigma/(\phi_D - \phi_Z)$]; the potential profiles are calculated by numerically solving Poisson's equation in 3D Fourier space. Figure 7 summarizes the behavior of C_D as O/C and σ are varied. In the pristine graphene case, it is evident that C_D tends to be around 125 to 135 F g^{-1}. However, as the O/C ratio of the electrode increases, C_D is predicted to diminish. Additionally, the suppression of C_D tends to be larger at the negative terminal, which exhibits as much as a 42% decrease in C_D as compared with the 35% decrease on the positive terminal side. Both of these observations are consistent with the aforementioned screening behavior, which tends to decrease as O/C increases, and more so near the negative electrode.

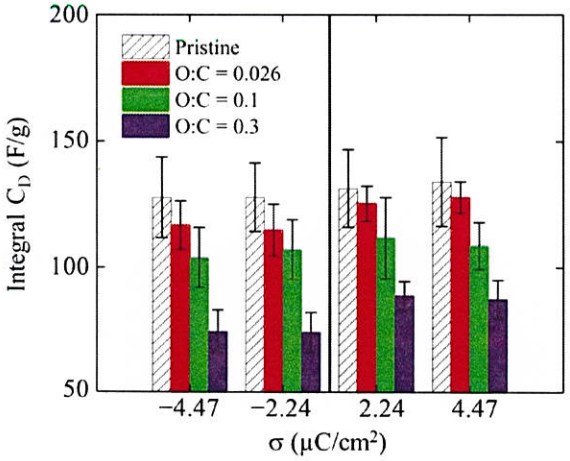

Figure 7. Comparison of the integral electric double-layer capacitances (C_D) for pristine graphene and three graphene oxide sheets with varying O/C ratios at the listed excess surface charge densities (σ).

2.3. Total Interfacial Capacitance

Having estimated the C_Q and C_D, we now compute the interfacial capacitance ($C_T = (1/C_Q + 1/C_D)^{-1}$). Figure 8 summarizes our results and shows that the C_T is enhanced by as much as 41% (33%) for positive (negative) polarity when using OH-functionalized electrodes with a O/C ratio of 0.1 as compared with that of pristine graphene; note that if $\sigma = \pm 4.47\ \mu C\,cm^{-2}$, the predicted operating voltage (ΔV) is 2.44 V for a C/O ratio of 0.1, which is much smaller than the value of 3.74 V predicted for the pristine graphene case. Despite the diminished C_D upon OH functionalization, we find that the C_T can be dramatically improved by virtue of the enhanced C_Q.

In addition, our results suggest that there may be an optimal O/C ratio at which the benefit from the C_Q most effectively mitigates the loss in C_D. However, there are several limitations in our simulations that prevent us from quantifying such a point. First, we did not take into account the charge smearing at the electrode–electrolyte interface, which may have underestimated our prediction of the C_D.[50] More importantly, the C_Q can be altered in the presence of other types of oxygen moieties, in addition to their concentrations and distributions across the basal plane. In particular, we should be wary of rGO sheets with bandgaps that have been predicted to be as large as 3.0 eV, which can occur when the O/C ratio is >0.5 for certain combinations and configurations of oxygen-containing functional groups.[38,51] Furthermore, the presence of additional topological defects that may be created through the rGO reduction process[52] can also strongly influence the electronic structure and the electrochemical stability. It is possible that the highly scattered performance of GO-based supercapacitors reported in the literature may be partially due to the structurally sensitive C_Q. Moreover, the possible suppression of electrical conductivity in rGO sheets with increased oxygen functionalization is another factor to consider.[22] Therefore, it will be important to improve both the experimental characterization and control of oxygen functionalization on rGO to utilize these materials fully for supercapacitor electrodes. Nonetheless, our study reveals that rGO materials, which are particularly attractive due to their ease of processing and scalability, can serve as a superior alternative to graphene electrodes for EDLC applications.

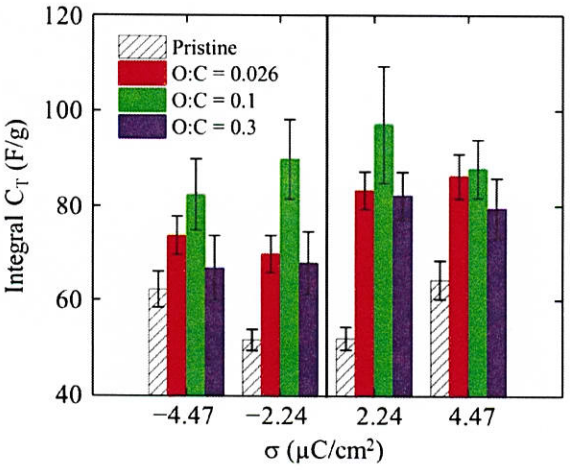

Figure 8. Comparison of the integral interfacial capacitances (C_T) for pristine graphene and three graphene oxide sheets with varying O/C ratios at the listed excess surface charge densities (σ).

3. Conclusions

We investigated the influence of reduced graphene oxide (rGO) electrodes immersed in [EMIM][FSI] ionic liquid on both the quantum (C_Q) and electric double-layer (C_D) capacitances by using a combined DFT and classical MD approach. As a model system, we only considered OH moieties along the basal plane, accounting for their preferential spatial agglomeration, and varied the ratio of OH to C (O/C). Our three primary conclusions are as follows:

- An increase in the O/C ratio (computed up to O/C 0.3) induces increased quasi-localization of C p_z states, which subsequently enhances the C_Q and electrochemical stability of OH on the basal surface.
- The C_D can be repressed as the O/C ratio increases, which we attribute to the unfavorable exchange of counterions with co-ions adjacent to the electrode surface due to the preferred two-dimensional ordering of cations and anions.
- The total interfacial capacitance ($C_T = [1/C_Q + 1/C_D]^{-1}$) of OH-functionalized electrodes is predicted to outperform pristine graphene electrodes owing to the mitigation of the suppressed C_D by improved C_Q; for example, when σ is 4.47 (-4.47) $\mu C\,cm^{-2}$, C_T is predicted to improve by 41% (33%).

Interestingly, our analysis suggests that the intended benefit from rGO electrodes strongly depends upon both the concentration and arrangement of oxygen species. This may help explain some inconsistencies reported in experimental results and advocates the need for careful control, characterization,

and optimization of oxygen functionalization. Nonetheless, our findings clearly demonstrate that the use of rGO materials can significantly improve C_T as compared with pristine graphene and, therefore, offer a promising alternative for supercapacitor devices.

Computational Methods

Electronic Structure Calculations

The electronic structure of each rGO sheet was calculated by using DFT within the Perdew–Berke–Ernzerhof generalized gradient approximation (GGA–PBE),[53] as implemented in the Vienna ab initio simulation package (VASP).[54] We employed the projector augmented wave (PAW) method[55] to describe the interaction between core and valence electrons, and a planewave basis set with a kinetic energy cutoff of 400 eV. The rGO sheet was modeled by using a 7×4 rectangular supercell (17.2648×17.0877 Å^2) with the PBE-optimized lattice constant of 2.466 Å for graphene. For all O/C ratios, *trans* pairs of OH groups were added to the graphene lattice according to the Metropolis Monte Carlo (MC) scheme described in the Supporting Information. Figure S1 depicts the number and size of distinct OH domains at varying O/C ratios and shows the tendency of O moieties to aggregate. For example, 68 OH groups (34 *trans* pairs) and 680 C atoms (O/C 0.1) forms five domains on average, with the largest domain covering 20% of the lattice. Periodic boundary conditions were employed in all three directions with a vacuum spacing of 20 Å in the vertical direction to separate the rGO sheet from its periodic images. For the Brillouin zone integration, we used a 6×6×1 Monkhorst–Pack (MP) *k*-point mesh[56] for geometry optimization and energy calculations and a 8×8×1 MP *k*-point mesh to ensure convergence for electronic structure calculations; all energy (force) calculations were converged to within 1×10^{-6} eV (0.02 eV Å^{-1}). For comparison, third-order self-consistent charge DFTB calculations were performed by using Slater–Koster parameters from Ref. [57] as implemented in the DFTB+ program.[58,59] A 13×13×1 MP *k*-point mesh was used for geometry optimization and electronic structure calculations with the same convergence tolerance.

For the C_Q calculations, larger rGO sheets (17×10 rectangular supercell corresponding to 41.9288×42.7193 Å^2) were prepared by using the same MC scheme with 9, 34, and 102 *trans* pairs of OH groups added to the lattice, to give O/C ratios of 0.026, 0.1, and 0.3, respectively. Here, a 5×5×1 MP *k*-point mesh was used for geometry optimization and electronic structure calculations. Partial atomic charges were computed by using Mulliken population analysis[60] for excess charge density $\sigma=0$, ±2.24, ±4.47 μC cm^{-2} (0, ±5, and ±10 e per sheet); these charges were used in the MD simulations, which are described below. All reported results were obtained from averages over five independent samples at each O/C ratio.

Molecular Dynamics Simulations

We employed MD simulations with the OPLS–AA force field[61,62] to determine the microstructure of [EMIM][FSI] and potential near pristine and selected rGO electrodes when $\sigma=0$, ±2.24, and ±4.47 μC cm^{-2}. As illustrated in Figure 9, the simulation domain consisted of 434 [EMIM][FSI] IL pairs surrounding an electrode (41.9288×42.7193 Å^2) with a depth of 86 Å in the *z* direction and periodic boundary conditions in all three directions; in the charged simulations, co-ions were removed from the domain to maintain charge neutrality. Note that the domain is large enough to obtain a bulk density of 1.43 g cm^{-3} far from the electrode, which is in agreement with previous simulation work.[40] The structure and charge distribution of the electrodes were determined from DFTB calculations, as described above. The force-field parameters for EMIM and FSI were adopted from Refs. [63] and [64], respectively. The Lennard–Jones (LJ) parameters for graphene and for the OH moieties were adopted from Refs. [65] and [61], respectively. Spherical cutoffs of 10 and 12 Å were used for the LJ and Coulomb interactions, respectively. Electrostatic interactions beyond the cutoff were calculated by using the Particle–Particle–Particle–Mesh solver.[66]

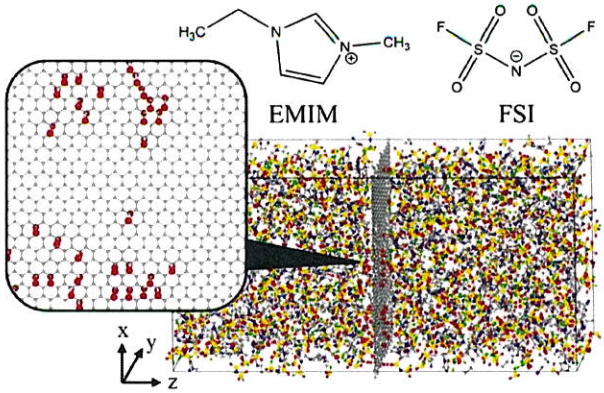

Figure 9. Schematic of EMIM/FSI ionic liquid (top) and the simulation domain used in classical molecular dynamics (bottom). The gray sheet in the middle corresponds to graphene oxide, which is shown magnified in the inset; gray, red, and white balls indicate C, O, and H atoms, respectively. Throughout the electrolyte, the gray, blue, and white balls correspond to C, N, and H atoms, respectively, in EMIM whereas the blue, yellow, red, and green balls correspond to N, S, O, and F atoms, respectively, in FSI.

Keeping the electrodes fixed, we annealed and quenched each MD simulation initially at 700 K for 3 ns followed by 2 ns at 350 K for two cycles (i.e. 10 ns total), and then further equilibrated for 3 ns at 300 K by using a 1 fs time step. Production runs were carried out for 4 ns with atomic positions recorded every 5 ps. All simulations were performed in the NVT ensemble with the temperature controlled by a Nosé–Hoover thermostat[67] with a 200 fs damping parameter. All MD simulations were performed by using the large-scale atomic/molecular massively parallel simulator (LAMMPS) program.[68] MD results reported herein were obtained from the average of five independent simulations with different initial atomic configurations.

Acknowledgements

This work was supported by a Korea CCS R&D Center (KCRC) grant (no. 2015053544) funded by the Korea government (Ministry of Science, ICT & Future Planning) and the Welch Foundation (F-1535). A.J.P. is grateful for support from the ECS Herbert H. Uhlig Summer Fellowship. We also thank the Texas Advanced Computing Center for use of the Stampede supercomputing system (OCI-1134872).

Keywords: capacitors · density functional calculations · ionic liquids · molecular dynamics · quantum capacitance

[1] P. Ribeiro, B. Johnson, M. Crow, A. Arsoy, Y. Liu, *Proc. IEEE* **2001**, *89*, 1744 – 1756.
[2] I. Hadjipaschalis, A. Poullikkas, V. Efthimiou, *Renewable Sustainable Energy Rev.* **2009**, *13*, 1513 – 1522.
[3] F. Béguin, V. Presser, A. Balducci, E. Frackowiak, *Adv. Mater.* **2014**, *26*, 2219 – 2251.
[4] P. Simon, Y. Gogotsi, *Acc. Chem. Res.* **2013**, *46*, 1094 – 1103.
[5] G. Xiong, C. Meng, R. G. Reifenberger, P. P. Irazoqui, T. S. Fisher, *Electroanalysis* **2014**, *26*, 30 – 51.
[6] J. Chen, C. Li, G. Shi, *J. Phys. Chem. Lett.* **2013**, *4*, 1244 – 1253.
[7] G. Wang, L. Zhang, J. Zhang, *Chem. Soc. Rev.* **2012**, *41*, 797 – 828.
[8] J. Xia, F. Chen, J. Li, N. Tao, *Nat. Nanotechnol.* **2009**, *4*, 505 – 509.
[9] M. D. Stoller, C. W. Magnuson, Y. Zhu, S. Murali, J. W. Suk, R. Piner, R. S. Ruoff, *Energy Environ. Sci.* **2011**, *4*, 4685 – 4689.
[10] E. Paek, A. J. Pak, G. S. Hwang, *J. Electrochem. Soc.* **2013**, *160*, A1 – A10.
[11] E. Paek, A. J. Pak, K. E. Kweon, G. S. Hwang, *J. Phys. Chem. C* **2013**, *117*, 5610 – 5616.
[12] A. J. Pak, E. Paek, G. S. Hwang, *Carbon* **2014**, *68*, 734 – 741.
[13] E. Paek, A. J. Pak, G. S. Hwang, *J. Electrochem. Soc.* **2014**, *161*, X15.
[14] E. Paek, A. J. Pak, K. E. Kweon, G. S. Hwang, *J. Phys. Chem. C* **2013**, *117*, 14461 – 14461.
[15] A. J. Pak, E. Paek, G. S. Hwang, *Carbon* **2014**, *77*, 1198 – 1198.
[16] J. Li, M. Östling, *Crystals* **2013**, *3*, 163 – 190.
[17] D. Chen, H. Feng, J. Li, *Chem. Rev.* **2012**, *112*, 6027 – 6053.
[18] Y. Zhu, D. K. James, J. M. Tour, *Adv. Mater.* **2012**, *24*, 4924 – 4955.
[19] S. Pei, H. M. Cheng, *Carbon* **2012**, *50*, 3210 – 3228.
[20] S. K. Bikkarolla, P. Cumpson, P. Joseph, P. Papakonstantinou, *Faraday Discuss.* **2014**, *173*, 415 – 428.
[21] B. Xu, S. Yue, Z. Sui, X. Zhang, S. Hou, G. Cao, Y. Yang, *Energy Environ. Sci.* **2011**, *4*, 2826.
[22] B. Zhao, P. Liu, Y. Jiang, D. Pan, H. Tao, J. Song, T. Fang, W. Xu, *J. Power Sources* **2012**, *198*, 423 – 427.
[23] P. Karthika, *Soft Nanosci. Lett.* **2012**, *02*, 59 – 66.
[24] Y. Chen, X. Zhang, D. Zhang, P. Yu, Y. Ma, *Carbon* **2011**, *49*, 573 – 580.
[25] T. Kim, H. C. Kang, T. T. Tung, J. D. Lee, H. Kim, W. S. Yang, H. G. Yoon, K. S. Suh, *RSC Adv.* **2012**, *2*, 8808 – 8812.
[26] L. Buglione, E. L. K. Chng, A. Ambrosi, Z. Sofer, M. Pumera, *Electrochem. Commun.* **2012**, *14*, 5 – 8.
[27] M. A. Pope, S. Korkut, C. Punckt, I. A. Aksay, *J. Electrochem. Soc.* **2013**, *160*, A1653 – A1660.
[28] A. D. DeYoung, S. Park, N. R. Dhumal, Y. Shim, Y. Jung, H. J. Kim, *J. Phys. Chem. C* **2014**, *118*, 18472 – 18480.
[29] S. Kerisit, B. Schwenzer, M. Vijayakumar, *J. Phys. Chem. Lett.* **2014**, *5*, 2330 – 2334.
[30] K. Xu, X. Ji, C. Chen, H. Wan, L. Miao, J. Jiang, *Electrochim. Acta* **2015**, *166*, 142 – 149.
[31] A. J. Pak, E. Paek, G. S. Hwang, *J. Phys. Chem. C* **2014**, *118*, 21770 – 21777.
[32] E. Paek, A. J. Pak, G. S. Hwang, *ACS Appl. Mater. Interfaces* **2014**, *6*, 12168 – 12176.
[33] A. Lerf, H. He, M. Forster, J. Klinowski, *J. Phys. Chem. B* **1998**, *102*, 4477 – 4482.
[34] W. Gao, L. B. Alemany, L. Ci, P. M. Ajayan, *Nat. Chem.* **2009**, *1*, 403 – 408.
[35] W. Cai, R. D. Piner, F. J. Stadermann, S. Park, M. A. Shaibat, Y. Ishii, D. Yang, A. Velamakanni, S. J. An, M. Stoller, J. An, D. Chen, R. S. Ruoff, *Science* **2008**, *321*, 1815 – 1817.
[36] K. Erickson, R. Erni, Z. Lee, N. Alem, W. Gannett, A. Zettl, *Adv. Mater.* **2010**, *22*, 4467 – 4472.
[37] S. Zhou, A. Bongiorno, *Sci. Rep.* **2013**, *3*, 2484.
[38] J.-A. Yan, M. Y. Chou, *Phys. Rev. B* **2010**, *82*, 125403.
[39] N. Handa, T. Sugimoto, M. Yamagata, M. Kikuta, M. Kono, M. Ishikawa, *J. Power Sources* **2008**, *185*, 1585 – 1588.
[40] O. Borodin, W. Gorecki, G. D. Smith, M. Armand, *J. Phys. Chem. B* **2010**, *114*, 6786 – 6798.
[41] B. C. Wood, T. Ogitsu, M. Otani, J. Biener, *J. Phys. Chem. C* **2014**, *118*, 4 – 15.
[42] C. Mattevi, G. Eda, S. Agnoli, S. Miller, K. A. Mkhoyan, O. Celik, D. Mastrogiovanni, G. Granozzi, E. Garfunkel, M. Chhowalla, *Adv. Funct. Mater.* **2009**, *19*, 2577 – 2583.
[43] J. Robertson, E. P. O'Reilly, *Phys. Rev. B* **1987**, *35*, 2946 – 2957.
[44] D. R. Dreyer, S. Park, C. W. Bielawski, R. S. Ruoff, *Chem. Soc. Rev.* **2010**, *39*, 228 – 240.
[45] K. Shimizu, A. Pensado, P. Malfreyt, A. A. H. Pádua, J. N. C. Lopes, *Faraday Discuss.* **2012**, *154*, 155 – 169.
[46] C. Merlet, D. T. Limmer, M. Salanne, R. van Roij, P. A. Madden, D. Chandler, B. Rotenberg, *J. Phys. Chem. C* **2014**, *118*, 18291 – 18298.
[47] S. Maolin, Z. Fuchun, W. Guozhong, F. Haiping, W. Chunlei, C. Shimou, Z. Yi, H. Jun, *J. Chem. Phys.* **2008**, *128*, 134504.
[48] S. A. Kislenko, I. S. Samoylov, R. H. Amirov, *Phys. Chem. Chem. Phys.* **2009**, *11*, 5584 – 5590.
[49] G. Feng, R. Qiao, J. Huang, S. Dai, B. G. Sumpter, V. Meunier, *Phys. Chem. Chem. Phys.* **2011**, *13*, 1152 – 1161.
[50] E. Paek, A. J. Pak, G. S. Hwang, *J. Chem. Phys.* **2015**, *142*, 024701.
[51] H. Huang, Z. Li, J. She, W. Wang, *J. Appl. Phys.* **2012**, *111*, 054317.
[52] A. Bagri, C. Mattevi, M. Acik, Y. J. Chabal, M. Chhowalla, V. B. Shenoy, *Nat. Chem.* **2010**, *2*, 581 – 587.
[53] J. P. Perdew, K. Burke, M. Ernzerhof, *Phys. Rev. Lett.* **1996**, *77*, 3865 – 3868.
[54] G. Kresse, J. Furthmüller, *Phys. Rev. B* **1996**, *54*, 11169 – 11186.
[55] P. Blöchl, *Phys. Rev. B* **1994**, *50*, 17953 – 17979.
[56] H. J. Monkhorst, J. D. Pack, *Phys. Rev. B* **1976**, *13*, 5188 – 5192.
[57] M. Gaus, A. Goez, M. Elstner, *J. Chem. Theory Comput.* **2013**, *9*, 338 – 354.
[58] M. Elstner, D. Porezag, G. Jungnickel, J. Elsner, M. Haugk, T. Frauenheim, S. Suhai, G. Seifert, *Phys. Rev. B* **1998**, *58*, 7260 – 7268.
[59] M. Gaus, Q. Cui, M. Elstner, *J. Chem. Theory Comput.* **2011**, *7*, 931 – 948.
[60] R. S. Mulliken, *J. Chem. Phys.* **1955**, *23*, 1833.
[61] W. L. Jorgensen, D. S. Maxwell, J. Tirado-Rives, *J. Am. Chem. Soc.* **1996**, *118*, 11225 – 11236.
[62] G. Kaminski, W. L. Jorgensen, *J. Phys. Chem.* **1996**, *100*, 18010 – 18013.
[63] N. Canongia Lopes, J. Deschamps, A. A. H. Pádua, *J. Phys. Chem. B* **2004**, *108*, 2038 – 2047.
[64] J. N. Canongia Lopes, K. Shimizu, A. A. H. Pádua, Y. Umebayashi, S. Fukuda, K. Fujii, S. Ishiguro, *J. Phys. Chem. B* **2008**, *112*, 9449 – 9455.
[65] L. Battezzati, C. Pisani, F. Ricca, *J. Chem. Soc. Faraday Trans. 2* **1975**, *71*, 1629 – 1639.
[66] R. W. Hockney, J. W. Eastwood, *Computer Simulation using Particles*, Taylor & Francis, Bristol, **1988**.
[67] W. Hoover, *Phys. Rev. A* **1985**, *31*, 1695 – 1697.
[68] S. Plimpton, *J. Comput. Phys.* **1995**, *117*, 1 – 19.

Manuscript received: February 5, 2016
Accepted Article published: February 17, 2016
Final Article published: February 26, 2016